Title

Acoustic Analysis and Sound Quality Assessment of a Quiet Helicopter for Air Taxi Operations

Journal

Journal of the American Helicopter Society, 67(3)

ISSN

0002-8711

Authors

Kevin Li, Sicheng
Lee, Seongkyu

Publication Date

2022-07-01

DOI

10.4050/jahs.67.032001

Acoustic Analysis and Sound Quality Assessment of a Quiet Helicopter for Air Taxi Operations

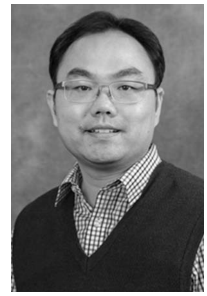

Sicheng (Kevin) Li*
Ph.D. Candidate

Seongkyu Lee
Associate Professor

Department of Mechanical and Aerospace Engineering
University of California, Davis, CA

This paper investigates tonal and broadband noise for rotor designs used on urban air mobility vehicles. Quiet helicopter rotor designs with varying tip speeds and blade numbers are studied for the tonal and broadband noise at the same mission specification. The rotor aerodynamics in edge-wise forward flight are calculated using the blade element theory coupled with a dynamic inflow model and the moment-balance trim analysis. Loading noise and thickness noise are obtained using the lifting-line loading distribution and the dual-compact thickness noise model in PSU-WOPWOP. With the forward flight capability developed in UCD-QuietFly, broadband noise, including trailing-edge noise, trailing-edge bluntness noise, and airfoil stall noise, is predicted. Psychoacoustic metrics, such as fluctuation and roughness, are used to quantify the human subjective annoyance levels. The relative importance between tonal noise and broadband noise is investigated for various design cases and operating conditions. It is found that broadband noise is the dominant noise source for the rotor designs with low tip speeds and fewer blades, while tonal noise is dominant for the high-tip-speed designs. A low tip speed and more blades are found to be the preferable design features in terms of psychoacoustic metrics.

Nomenclature

A_{cs}	airfoil cross-sectional area, m^2
C_T	rotor thrust coefficient
C_f	skin friction coefficient
c	chord length, m
c_0	speed of sound in undisturbed medium, m/s
dP/dx	streamwise surface pressure gradient, Pa/m
$\mathbf{F}$	fluctuation strength, vacil
f	frequency, Hz
f_{mod}	modulations frequency, Hz
H_j^r	factorial combination
i	blade section index
j, n	polynomial number (shape function index)
L_{BBN}	broadband noise level, dB
$[L]$	influence matrix
L_i^q	lift on the qth blade ith section, N
ΔL	overall modulation depth, dB
ΔL_E	specific modulation depth, dB/Bark
l_M	blade surface loading in the motion direction, $\vec{l} \cdot \hat{M}$, N/m
l_r	blade surface loading in the radiation direction, $\vec{l} \cdot \hat{r}$, N/m
$\vec{l}$	blade surface loading vector, N/m
M_r	March number in the radiation direction, $\vec{M} \cdot \hat{r}$
$[M]$	apparent mass matrix
m	modulation factor
N_q	number of blades
N_i	number of sections per blade
$(n)!!$	double factorial of n, $(n)(n-2)(n-4), \ldots$
OASPL	overall sound pressure level, dB
p'	total acoustics pressure, Pa
p'_L	loading noise acoustic pressure, Pa
p'_T	thickness noise acoustic pressure, Pa
q	blade index
$\mathbf{R}$	roughness, asper
R	rotor radius, m
r_0	distance between $\vec{y}$ and $\vec{x}$, m
r_1	blade section radial location, m
$\hat{r}$	unit vector in the radiation direction
$\bar{r}$	non-dimensional blade radial location
r, m	harmonic number
SPL	sound pressure level, dB
t	observer time, s
$\bar{t}$	non-dimensional time, Ωt
U_e	boundary layer edge velocity, m/s
V_i	inflow velocity, m/s
V_∞	rotor forward velocity, m/s
w	inflow ratio, $V_i/\Omega R$
X_2, Y_2, Z_2	observer global coordinate system
$\vec{x}$	observer position, m

*Corresponding author; email: sili@ucdavis.edu.

Presented at the Vertical Flight Society 77th Annual Forum & Technology Display, Virtual Event, May 11–13, 2021. Manuscript received August 2021; February 2022.

DOI: 10.4050/JAHS.67.032001

$\vec{y}$	sound source position, m
α_j^r, β_j^r	induced flow coefficients
α_{sh}	rotor shaft angle of attack, deg
α_{tpp}	rotor tip-path-plane angle of attack, deg
δ^*	boundary layer displacement thickness, m
μ	advance ratio
ν	local fluid velocity on the blade surface, m/s
ν_n	normal component of fluid velocity, m/s
ρ_0	air density in undisturbed medium, kg/m^3
τ	source time, s
τ_n^m	loading coefficients
ϕ_j^r	radial expansion function
ψ	azimuth angle, deg
Ω	rotational speed, rad/s

Introduction

Urban air mobility (UAM) is a concept in which passengers and cargo are transported in urban areas mainly using vertical takeoff and landing (VTOL) aircraft. Multiple VTOL designs have been created in recent years. For example, Silva et al. (Ref. 1) at NASA designed three configurations, such as quadcopter, side-by-side, and lift-cruise, with the same mission specifications of carrying six passengers. A recent multidisciplinary optimization (Ref. 2) of NASA's eVTOL conceptual designs (Ref. 1) shows that the minimum cruise flight altitude should be about 1700 ft. Although many UAM aircraft designs have multirotor configurations with a distributed power system, Johnson (Ref. 3) presented a quiet single-rotor helicopter for urban air taxi operations, as shown in Fig. 1. A quiet helicopter was designed with variations of the number of blades, solidity, and RPM. Key attributes of this quiet helicopter are the muffled propulsion system and a no tail rotor-style tailboom to eliminate high-frequency tail rotor noise. Scott (Ref. 4) investigated eVTOL aircraft configurations for military mission requirements. He found that a traditional low disk loading configuration, such as a coaxial rotor, provides the best operational benefits among various eVTOL configurations including multirotors and ducted fans. Johnson's and Scott's studies provide different perspectives on eVTOL configurations and reinforce the importance of the traditional low disk loading helicopter, although multirotor configurations are still a dominant choice being developed by many companies (Refs. 5 and 6). However, there are limited understanding and studies on noise, sound quality, and annoyance levels of this quiet helicopter in the context of UAM and public acceptance.

NASA UAM market study (Ref. 7) presented that noise is one of the top potential barriers to a successful UAM market due to its negative public acceptance. Uber (Ref. 8) suggested that UAM VTOL vehicles should have a noise level (L_{Amax}) less than 62 dB(A) at an altitude of 500 ft or 67 dB(A) at 250 ft, and it has been demonstrated that these noise targets can be challenging to meet with the current VTOL aircraft designs (Refs. 9, 10, 11). Numerous computational studies have been performed recently to analyze multirotor VTOL aircraft and drone noise. Tonal noise of quadrotor and side-by-side configurations of VTOL aircraft were studied using high-fidelity CFD (Refs. 11–13). Pettingill and Zawodny (Ref. 14) investigated broadband noise of small-scale drone rotors using the Brooks-Pope-Marcolini (BPM) model (Ref. 15). Thurman et al. (Ref. 16) used the lattice-Boltzmann method–very-large-eddy simulation to predict noise from a DJI-9450 drone rotor in hover, and they found that broadband noise is the dominant noise source above 1 kHz. Smith et al. (Ref. 17) studied the effect of increasing the number of rotors on multicopter tonal noise using the rotor aerodynamics software Rensselaer Multicopter Analysis Code (Ref. 18) and the acoustics software PSU-WOPWOP (Refs. 19, 20).

By its frequency characteristics, rotorcraft noise can be categorized into tonal and broadband noise, where rotor tonal noise is important in the forward direction (Ref. 21), while rotor broadband noise mainly propagates in the downward (or plane-normal) direction (Ref. 22). Rotor tonal noise is the dominant noise source at the low- and midfrequency ranges and has discrete-frequency characteristics. It consists of various sources, such as steady loading noise, thickness noise, unsteady blade–vortex-interaction (BVI) noise, and high-speed impulsive noise. Loading noise is generated by the forces to the fluid caused by the moving body, while thickness noise is generated by the displacement of fluid due to the body motion. Loading and thickness noise can be solved by the computation of Farassat's formulation 1A (Refs. 23, 24) of the Ffowcs Williams and Hawkings (FW-H) equation (Ref. 25). This method is widely used in acoustic simulation software, including PSU-WOPWOP (Refs. 19, 20) and ANOPP (Ref. 26). At the onset of BVI noise, it becomes the most dominant tonal noise, so the accurate prediction of the blade and vortex interaction is critical to assessing UAM noise. High-speed impulsive noise associated with shock waves and the nonlinear sound propagation are important at high Mach number flows (Ref. 27), but this type of noise can be easily avoided on the low-tip-speed UAM aircraft. In general, it is straightforward and feasible to predict rotor tonal noise with low- or medium-fidelity solvers when BVI noise is not present.

Rotorcraft tonal noise has been studied through experiments and computations. Thickness noise and loading noise were measured in the acoustics wind tunnel (Ref. 28), and the BVI noise was studied in the flight test (Ref. 29). High-fidelity computational fluid dynamics (CFD) has the capability of investigating tonal noise on the complex vehicle configurations, such as the rotor-to-rotor and rotor-to-wing interactions (Refs. 30, 21). On the other hand, the low-fidelity approaches are shown to capture tonal noise and thickness noise with low computational costs. The free-wake model and vortex-particle method were used to calculate the rotor blade loading for the FW-H solver (Refs. 31–33). The finite state dynamic inflow model was used to calculate rotor forward flight aerodynamics that was used in the FW-H solver to predict tonal noise at the blade passing frequency (Refs. 34, 35). Blade element theory, coupled with the FW-H solver, was also used on an axial flight propeller to predict tonal noise (Ref. 36).

Historically, more research efforts have been devoted to tonal noise compared to broadband noise in the rotorcraft community, since conventional helicopters operate at high tip Mach numbers where tonal noise is important. However, the thriving UAM market has brought to the rotorcraft community a significant interest in broadband noise due to the reduced tip speeds and close proximity to residential areas (Ref. 37). Rotor broadband noise in large scale typically dominates at the mid- to high-frequency range (Ref. 38) (1–5 kHz), which is in a sensitive frequency range in human hearing, as manifested in the A-weighting (Ref. 39).

The prediction models of rotorcraft broadband noise are mainly based on two different approaches: the physics-based acoustics model and the empirical noise model. First, the physics-based acoustics models, such as the Amiet model (Ref. 40) and the Howe model (Ref. 41), are developed from the theories of edge scattering of pressure fluctuations on an airfoil. As for their advantages, these models account for fundamental physics of the noise generation mechanism (Ref. 42), which provides the ability to accurately predict noise in general airfoils, such as cambered airfoils, and flow conditions as well as the flexibility to investigate complicated acoustic scattering processes, such as the serrated trailing edge (Ref. 43). However, the physics-based models still depend on the input of the wall pressure spectrum (Ref. 44) near the trailing edge. The Amiet model has been used to study broadband noise on helicopters, propellers, axial fans, and wind turbines (Refs. 22, 45–49). Second, the empirical broadband noise models are determined by curve fitting the measured broadband noise in conjunction with a proper scaling, such as

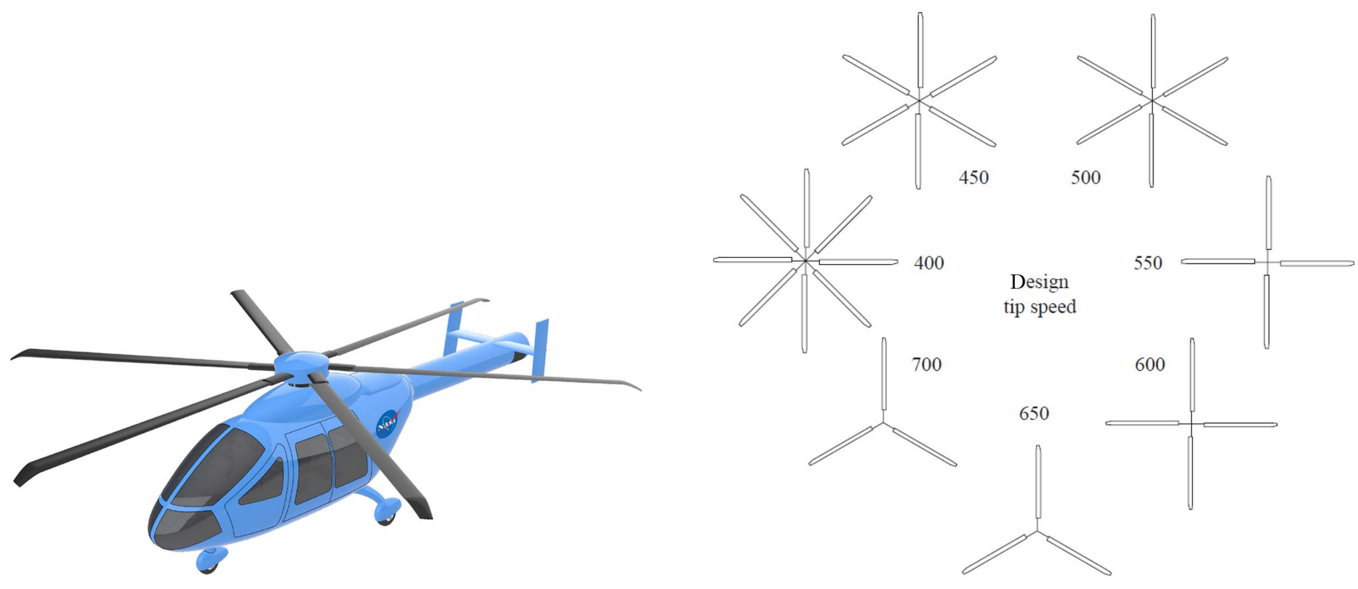

(a) **(b)**

Fig. 1. Quiet helicopter (a) configuration and (b) rotor geometry for various design tip speeds (Ref. 3).

the semiempirical BPM model (Ref. 15). These empirical models tend to accurately predict broadband noise for the airfoils that were used in the model development, but they reveal little noise mechanisms and require additional measurements for different airfoils, such as cambered airfoils. Based on the BPM model, rotor broadband noise has been predicted and validated against the experiments (Ref. 39, 50–54).

For UAM VTOL in the hovering flight, we developed a computational toolchain to predict rotor broadband noise, namely the UCD-QuietFly (Refs. 22, 9). This tool predicts rotor trailing-edge broadband noise, which combines blade element momentum theory (BEMT), XFOIL panel method (Ref. 55), Lee's wall pressure spectrum model (Ref. 44), and Amiet's trailing-edge noise model (Ref. 40). This prediction method considers rotor blades' full motions. The rotorcraft aerodynamics is solved by the BEMT to obtain the local velocity and angle of attack along the blade span. For each blade section, the far-field noise is obtained from the Amiet trailing-edge noise model, which requires the coordinate transformations to include rotor blade motions.

In this paper, the recent developments in UCD-QuietFly are presented to predict rotorcraft broadband noise in trimmed forward flight with the applications to UAM aircraft. The trimmed rotor forward flight aerodynamics is calculated using the Peters–He dynamic inflow model (Ref. 56), the force-moment balance trim solution (Ref. 57), and the blade element theory. With the updated UCD-QuietFly capabilities, we are able to investigate NASA's newly designed quiet helicopter noise in forward flight with varying tip speeds and blade numbers at various operating conditions. The relative importance of tonal noise and broadband noise is investigated in this paper. The psychoacoustic metrics of time-varying broadband noise are also studied.

Method and Formulation

This section presents the Peters–He dynamic model to calculate the inflow of a trimmed rotor in steady forward flight. Next, rotor tonal and broadband noise prediction approaches are presented. As the detailed theories in UCD-QuietFly can be found in Refs. 9, 22, and 58, the newly developed theories in UCD-QuietFly in forward flight are only presented in this section. Lastly, psychoacoustic metrics, such as fluctuation strength and roughness, that assess the subjective annoyance levels are briefly described.

Rotor airloads and inflow prediction

The inflow distribution of a trimmed forward flight is calculated using the Peters–He dynamic inflow model (Ref. 56). The normalized inflow velocity w shown in Eq. (1) is written as a combination of multiple states,

$$w(\bar{r}, \psi, \bar{t}) = \sum_{r=0}^{\infty} \sum_{j=r+1,r+3...}^{\infty} \phi_j^r(\bar{r})\left[\alpha_j^r(\bar{t}) \cos r\psi + \beta_j^r(\bar{t}) \sin r\psi\right] \quad (1)$$

where ϕ is the radial expansion shape function, ψ is the azimuth angle, $\bar{t}$ is the nondimensional time, $\bar{r}$ is the nondimensional radial location, and α and β are the induced flow coefficients to be determined in the model. The radial shape function $\phi(\bar{r})$ is described as

$$\phi_j^r(\bar{r}) = \sqrt{(2j+1)H_j^r} \sum_{q=r,r+2,...}^{j-1} \bar{r}^q \frac{(-1)^{(q-r)/2}(j+q)!!}{(q-r)!!(q+r)!!(j-q-1)!!} \quad (2)$$

with

$$H_j^r = \frac{(j+r-1)!!(j-r-1)!!}{(j+r)!!(j-r)!!} \quad (3)$$

where r and j are the harmonic and polynomial numbers. The double factorial is defined as $(n)!! = n(n-2)(n-4)....$

The induced flow coefficients are formulated in Eq. (4), where * means the time derivative and the τ_n^m vectors contain the rotor loading coefficients. In a trimmed steady forward flight, the unsteady coefficients α^* and β^* are zeros, and the loading coefficients are averaged over one rotor revolution. $[M]$ and $[L]$ are the apparent mass matrix and the influence matrix that can be found in Ref. 56.

$$\begin{aligned}
&[M]\begin{bmatrix} \vdots \\ \{\alpha_j^r\} \\ \vdots \end{bmatrix}^* + [L^c]^{-1}\begin{bmatrix} \vdots \\ \{\alpha_j^r\} \\ \vdots \end{bmatrix} = \begin{bmatrix} \vdots \\ \{\tau_n^m\}^c \\ \vdots \end{bmatrix} \\
&[M]\begin{bmatrix} \vdots \\ \{\beta_j^r\} \\ \vdots \end{bmatrix}^* + [L^s]^{-1}\begin{bmatrix} \vdots \\ \{\beta_j^r\} \\ \vdots \end{bmatrix} = \begin{bmatrix} \vdots \\ \{\tau_n^m\}^s \\ \vdots \end{bmatrix}
\end{aligned} \quad (4)$$

On the right-hand side of Eq. (4), the loading coefficient matrices can be expressed in Eq. (5), where q is the blade index, i is the blade element index, and L_i^q is the rotor normal force on the qth blade and ith section. The same shape function shown in Eq. (2) is used in Eq. (5) with r and j replaced by m and n. The rotor normal force and the inflow ratio are interdependent and solved iteratively to find a solution in trimmed forward flights.

$$\tau_n^{0c} = \frac{1}{2\pi\rho_0\Omega^2 R^4}\sum_{q=1}^{N_q}\left[\sum_{i=1}^{N_i} L_i^q \phi_n^m(\bar{r}_i)\right]$$
$$\tau_n^{mc} = \frac{1}{\pi\rho_0\Omega^2 R^4}\sum_{q=1}^{N_q}\left[\sum_{i=1}^{N_i} L_i^q \phi_n^m(\bar{r}_i)\right]\cos(m\psi) \quad (5)$$
$$\tau_n^{ms} = \frac{1}{\pi\rho_0\Omega^2 R^4}\sum_{q=1}^{N_q}\left[\sum_{i=1}^{N_i} L_i^q \phi_n^m(\bar{r}_i)\right]\sin(m\psi)$$

The helicopter control settings or trim solutions for the various designs and flight operations are found using the force-moment-balance method (Ref. 57), which is a low-fidelity model for trim flights.

Tonal noise prediction

The exact equations of Farassat's formulation 1A that consist of thickness noise p'_T and loading noise p'_L are given as

$$p'(\vec{x}, t) = p'_T(\vec{x}, t) + p'_L(\vec{x}, t) \quad (6)$$

$$4\pi p'_T(\vec{x}, t) = \int_{f=0}\left[\frac{\rho_0(\dot{v}_n + v_{\dot{n}})}{r_0|1-M_r|^2}\right]_{ret} dS + \int_{f=0}\left[\frac{\rho_0 v_n(r_0\dot{M}_r + c(M_r - M^2))}{r_0^2|1-M_r|^3}\right]_{ret} dS \quad (7)$$

$$4\pi p'_L(\vec{x}, t) = \frac{1}{c}\int_{f=0}\left[\frac{\dot{l}_r}{r_0|1-M_r|^2}\right]_{ret} dS + \int_{f=0}\left[\frac{l_r - l_M}{r_0^2|1-M_r|^2}\right]_{ret} dS + \frac{1}{c}\int_{f=0}\left[\frac{l_r(r_0\dot{M}_r + c(M_r - M^2))}{r_0^2|1-M_r|^3}\right]_{ret} dS \quad (8)$$

The acoustics software PSU-WOPWOP (Ref. 19) will be used to predict the compact loading noise and compact thickness noise. The blade local loading l that is integrated along the chord, which is a function of the blade radial location and the azimuth angle, is calculated by the blade element theory (BET) for the trimmed forward flight condition using the dynamic inflow model described in the previous subsection. The azimuthally varying loading yields the unsteady loading derivative, $\dot{l}$, at each time step. To calculate the thickness noise, the dual-compact thickness noise formulation (Ref. 59) is used. The loading noise term shown in Eq. (8) can be used to calculate the thickness noise by integrating the constant loading ($\rho_0 c_0^2$) on two lines that represent a rotor blade (Ref. 59). This approach essentially follows Isom's thickness noise computation (Ref. 60). This dual-compact thickness noise formulation was implemented in PSU-WOPWOP (Ref. 19), where rotor thickness noise can be calculated given the blade motion, airfoil shape, and radial location. Therefore, rotor thickness noise is conveniently predicted without calculating the blade surface integral.

Broadband noise prediction

Rotor broadband noise is predicted using UCD-QuietFly (Refs. 9, 22, 58), whose architecture is shown in Fig. 2. The airfoil-self noise sources, including trailing-edge noise, trailing-edge bluntness noise, and airfoil stall noise, are predicted based on each blade section and summed for the entire rotor. Obtained from the trimmed rotor forward flight analysis, the time-dependent blade local velocity $U_\infty(r_1, \psi, q)$ and angle of attack $AoA(r_1, \psi, q)$ are the inputs to UCD-QuietFly, where r_1 is the blade radial position, ψ is the azimuth angle, and q is the blade index.

One important update in UCD-QuietFly is the addition of rotor broadband noise predictive capability in forward flight. The source time τ of each blade section is associated with the angular velocity Ω and azimuthal angle ψ by

$$\tau = \frac{\psi}{\Omega} \quad (9)$$

At the given source time and location, the observer time and location are obtained in the following equation:

$$t - \frac{|\vec{x}(t) - \vec{y}(\tau)|}{c} - \tau = 0 \quad (10)$$

where $\vec{x}(t)$ is the observer coordinate at the observer time t, and $\vec{y}(\tau)$ is the blade section coordinate at the source time τ. A schematic of a two-bladed rotor in forward flight and a moving observer with the same forward velocity is shown in Fig. 3.

According to Fig. 3, the distance of $|\vec{x}(t) - \vec{y}(\tau)|$ required in Eq. (10) is calculated as

$$|\vec{x}(t) - \vec{y}(\tau)| = \sqrt{[(X_2 - r_1\cos\psi\cos\alpha_{sh}) + V_\infty(t-\tau)]^2 + [Y_2 - r_1\sin\psi\cos\alpha_{sh}]^2 + [Z_2 - r_1\cos\psi\sin\alpha_{sh}]^2} \quad (11)$$

where ψ and α_{sh} are the rotor azimuth angle and shaft angle of attack, respectively. To calculate the observer time of each blade section, the quadratic equation shown in Eq. (10) is solved using the Newton–Raphson root finding method. Although Eq. (10) can be applicable to a stationary or arbitrarily moving observer, we use an observer that moves along with the vehicle throughout this paper.

The broadband noise of each blade section is calculated in terms of the sound pressure level SPL(f, τ) at the source time (τ), and the sound pressure level SPL(f, t) at the observer time is saved at the observer time (t), which is found in Eq. (10). This observer time would be different at each blade section. After the calculations of SPL at every time step and blade section, the sound pressure levels at the same observer time t are interpolated and summed to have total broadband noise. As a result, we obtain broadband noise as a function of the observer time, which is necessary to evaluate the amplitude modulation of noise and psychoacoustic metrics.

Psychoacoustic metrics

A time variation of broadband noise causes the fluctuations of noise amplitude, which affect the subjective human annoyance. Understanding and quantifying subjective annoyance is important for designing a new low-noise helicopter. In order to assess the annoyance levels, we use two psychoacoustic metrics: fluctuation strength and roughness. Based on the psychoacoustic models developed by Fastl and Zwicker (Ref. 61), the noise fluctuations with the modulation frequency under 20 Hz are categorized as the amplitude modulations, while the fluctuations with the modulation frequency over 20 Hz are categorized as roughness.

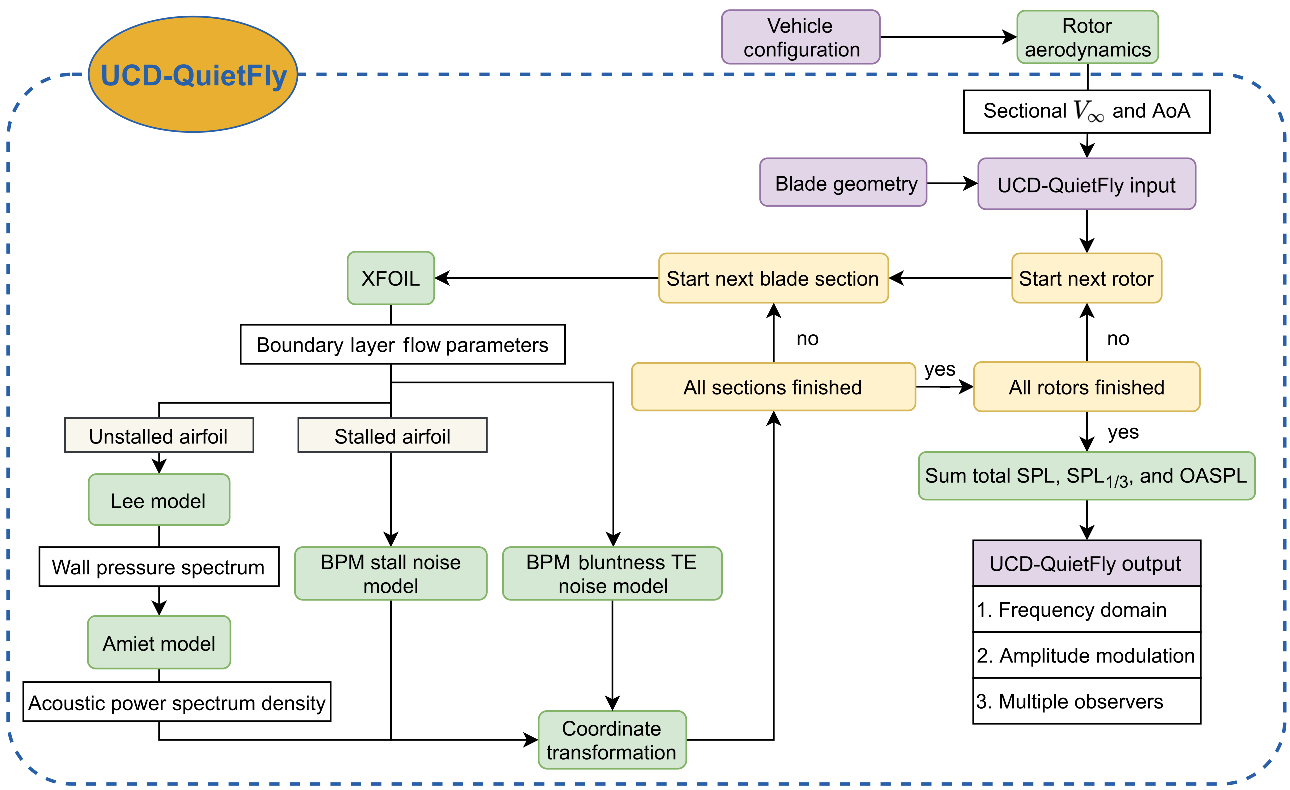

Fig. 2. Rotor broadband noise prediction code UCD-QuietFly flowchart.

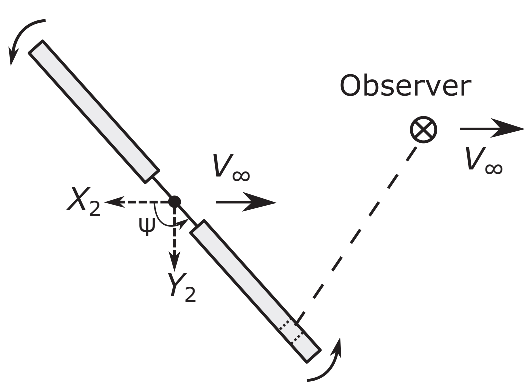

Fig. 3. Top view of a two-bladed rotor in forward flight.

The fluctuation strength is calculated using Eq. (12).

$$\mathbf{F} = \frac{5.8(1.25m - 0.25)[0.05(L_{\mathrm{BBN}}) - 1]}{(f_{\mathrm{mod}}/5)^2 + (4/f_{\mathrm{mod}}) + 1.5} \quad \text{vacil} \tag{12}$$

where L_{LBB} is the broadband noise overall sound pressure level (OASPL), f_{mod} is the modulation frequency in Hertz, and m is the modulation factor determined from the overall modulation depth, or the peak-to-peak amplitude, $\Delta L = 20\log[(1+m)/(1-m)]$. The modulation frequency is taken as the blade passing frequency. When the modulation depth is less than 3.52 dB, the fluctuation strength **F** becomes negative and negligible.

The roughness is calculated using Eq. (13).

$$\mathbf{R} = 0.3\frac{f_{\mathrm{mod}}}{1000}\int_0^{24\mathrm{Barks}} \Delta L_E(z)dz \quad \text{asper} \tag{13}$$

where $\Delta L_E(z)$ is the specific modulation depth at the zth critical band, which is integrated on the 24 bands (Barks) of the frequency spectrum. In the current study, the critical bands are approximated by the one-third-octave bands.

Validations

This section briefly presents the validations of the inflow distribution in forward flight using the Peters–He dynamic inflow model, tonal noise using PSU-WOPWOP, and broadband noise using UCD-QuietFly against various rotor experimental data. The validation cases and the prediction accuracy of each method are demonstrated.

Rotor inflow validation

Figure 4 shows the validation of the inflow on the rotor disk in forward flight for a 2-Meter Rotor Test System (2MRTS) rotor using the Peters–He model (Ref. 56). The prediction is validated against the inflow measured by the laser velocimeter (Ref. 62). It is shown that the predicted inflow distribution agrees well with the measurement, especially on the blade tip sections that significantly contribute to broadband noise. The validation of the inflow distribution is also important for tonal noise predictions since the inflow velocity determines the local angle of attack, which provides the blade sectional loading from the two-dimensional airfoil aerodynamics.

The inflow predictions at the hub region show some discrepancies to the experiment, but due to the low speed and lower loading, the inboard sections are considered less important to tonal noise and broadband noise. The discrepancies at the hub region are mainly due to the flow separation and reverse flow on the retreating blade's inboard sections. More validations of the current model can be found in Ref. 63. At the tip region, which is important in tonal and broadband noise, the predictions show good agreement with the experimental data.

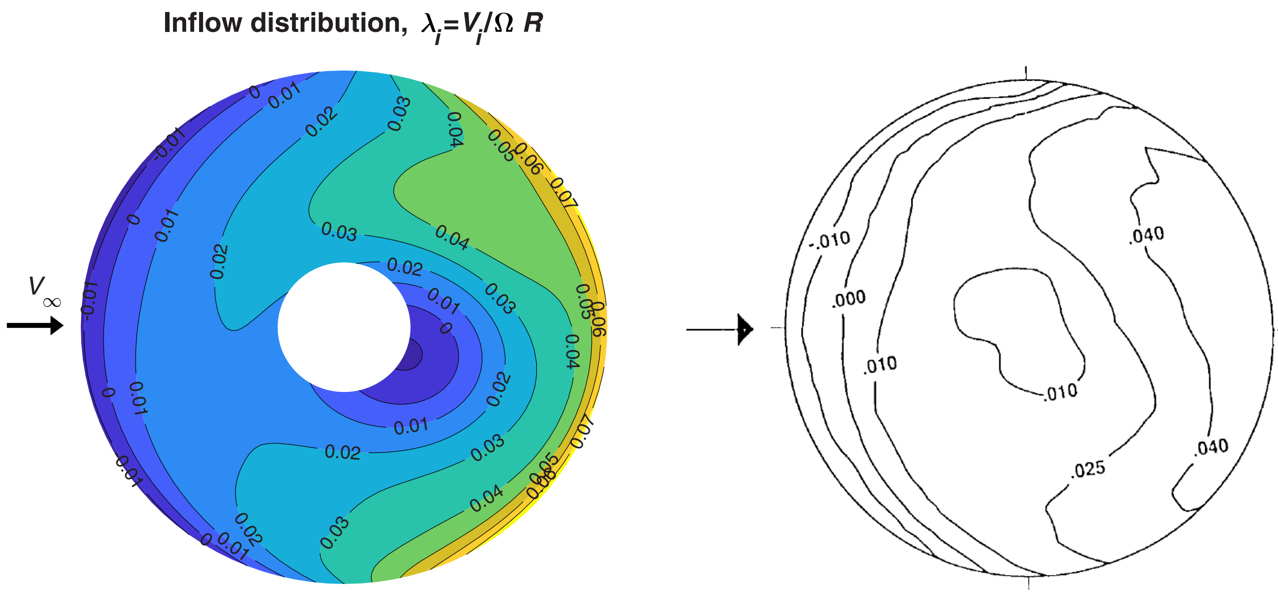

(a) (b)

Fig. 4. Validation of rotorcraft forward flight inflow distributions on 2MRTS rotor at μ = 0.15: (a) prediction, and (b) measurement (Refs. 62, 56).

Table 1. Validation rotor cases

Parameter	Case 1 (Ref. 28)	Case 2 (Ref. 28)	Case 3 (Ref. 37)
Rotor name	BO105	BO105	Bell430
Scale	40%	40%	full
Rotor radius (ft)	6.56	6.56	21
Number of blades	4	4	4
RPM	1050	525	349
Advance ratio	0.086	0.173	0.27
Thrust coefficient	0.0044	0.0044	0.0047
Observer-hub distance (ft)	23.4	23.4	492
Observer elevation angle (deg)	90	90	−90

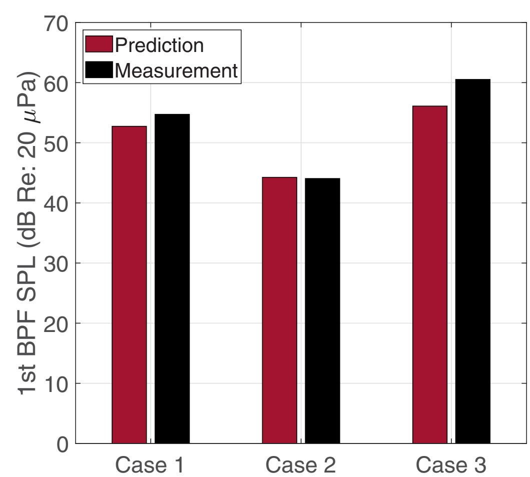

Fig. 5. Validations of tonal noise predictions, compared with the measurements of Brooks et al. (Ref. 28) and Snider et al. (Ref. 37). Rotor specifications and observer locations are given in Table 1.

Tonal noise validation

Figure 5 shows the validations of the tonal noise predictions by using the rotor airloads in forward flight obtained from the BET code above in PSU-WOPWOP. The validations are performed on the BO105 and Bell430 rotors, whose properties are shown in Table 1. The three rotor cases are selected to validate noise in different ranges of the rotor scale, the tip speed, and the advance ratio. The 40% scale BO105 rotor acoustic measurements (cases 1 and 2) were carried out by Brooks et al. (Ref. 28) in the Duits–Nederlandse Wind Tunnel in the forward flight conditions. The helicopter flight test of Bell430 (case 3) was performed by Snider et al. (Ref. 37) to obtain the measured noise data. Since the forward flight analysis does not include BVI, only the first blade passing frequency (BPF) noise level is compared between simulations and measurements. It is shown that the predictions agree well with the experimental data for all the three cases.

Broadband noise validation

Since UCD-QuietFly has been extensively validated on various rotor cases with different scales (Refs. 9, 22, 58, 45) in hover flights, only one additional validation case is shown in this paper in Fig. 6 for the BO-105 40% scale rotor (case 2) in forward flight. The narrow-band SPL prediction of broadband noise is compared with the wind tunnel acoustic measurements (Ref. 28). The comparison confirms that the predictions from UCD-QuietFly well capture the measured noise levels in the mid- to high-frequency range (2–15 kHz) on the noise spectrum, where airfoil-self broadband noise, such as trailing-edge noise, is dominant. The frequency range below 2 kHz is dominated by other noise sources, such as blade-wake-interaction (BWI) noise and tonal noise. While the prediction method of tonal noise is presented in the previous section, BWI noise is not included in this study.

Results

The quiet air taxi designs are investigated in this paper for their tonal noise, broadband noise, and psychoacoustic analyses. Table 2 shows the

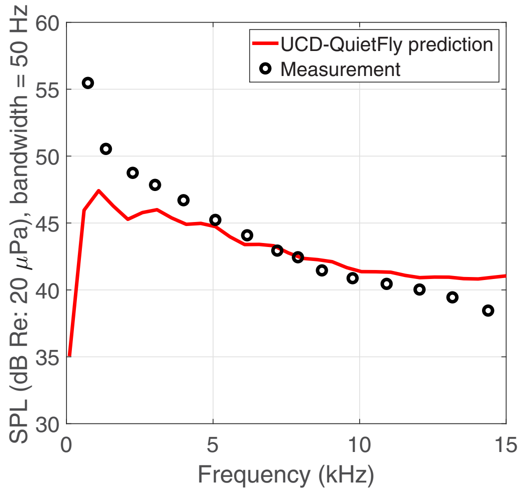

Fig. 6. Validation of UCD-QuietFly on forward flight rotor of Case 2 shown in Table 1, compared with the measurement of Brooks et al. (Ref. 28). RPM = 525, $\mu = 0.173$, $\alpha_{tpp} = -10°$, $C_T = 0.044$, and observer at 23.4 ft directly above the rotor.

quiet air taxi conceptual configurations designed by Johnson (Ref. 3) with different rotational tip speeds while maintaining the same disk loading and forward speed. With the reduced blade tip speed, the rotor solidity is increased by increasing the number of blades to maintain the same payload. Therefore, the acoustics analysis in this paper includes the combined effects of multiple designs and operating parameters. The current study shows the acoustic analysis at the same mission specification with different rotor blade designs. The blade sectional loading force and derivative at 75% radial location are shown in Fig. 7 for the seven configurations. As the number of blades increases, the loading force on one blade decreases. With the same number of blades, the lower tip speed design has the slightly higher loading force because of the larger chord length. The higher tip speed design gives the higher loading derivative, which results in the higher loading noise from one blade.

Tonal and broadband noise comparison

The tonal and broadband noise predictions at the downward position are shown in Fig. 8, where A-weighting is applied for the adjustment of human hearing. The total noise level is the logarithmic summation of tonal and broadband noise. It is seen that the high tip speed designs of 700, 650, 600, and 550 ft/s rotors have higher tonal noise levels than the lower tip speed designs due to the increased blade loading derivative and the associated loading noise. Thickness noise is weak when the observer is directly beneath the rotor. However, an increase in tonal noise is observed from the tip speed of 650–600 ft/s, and from 500 to 450 ft/s, due to the acoustic destructive and constructive interferences between the blades, which will be discussed later. On the other hand, since broadband noise is highly dependent on the tip speed, the broadband noise level is observed to decrease linearly with decreasing the rotor tip speed. For the designs with the tip speeds of 550 and 600 ft/s, the tonal noise OASPL is higher than that of broadband noise, while the broadband noise level significantly exceeds tonal noise for the low tip speed designs. In the current study, since tonal noise is dominated by the first BPF, which is less than 100 Hz, A-weighting significantly reduces the tonal noise levels as shown in Fig. 8(b). However, since broadband noise has its peak levels near 2 kHz frequency, A-weighting has little effect on its noise levels. Therefore, broadband noise is demonstrated to be the dominant noise source in terms of human hearing at the downward position.

A recent study by Silva and Johnson, which examined these seven helicopter designs in flyover, showed that reducing the tip speed significantly reduces the effective perceived noise level until 500 ft/s, while the noise reduction is less effective below that tip speed (Refs. 54, 3). However, they did not show the detailed breakdown of noise levels or an in-depth study on the noise trends. We observed a similar trend in Fig. 8, where the noise level is greatly reduced from the tip speed of 550 to 500 ft/s, and the noise reduction is ineffective below 500 ft/s tip speed. This sudden noise drop at 500 ft/s is due to the change of the number

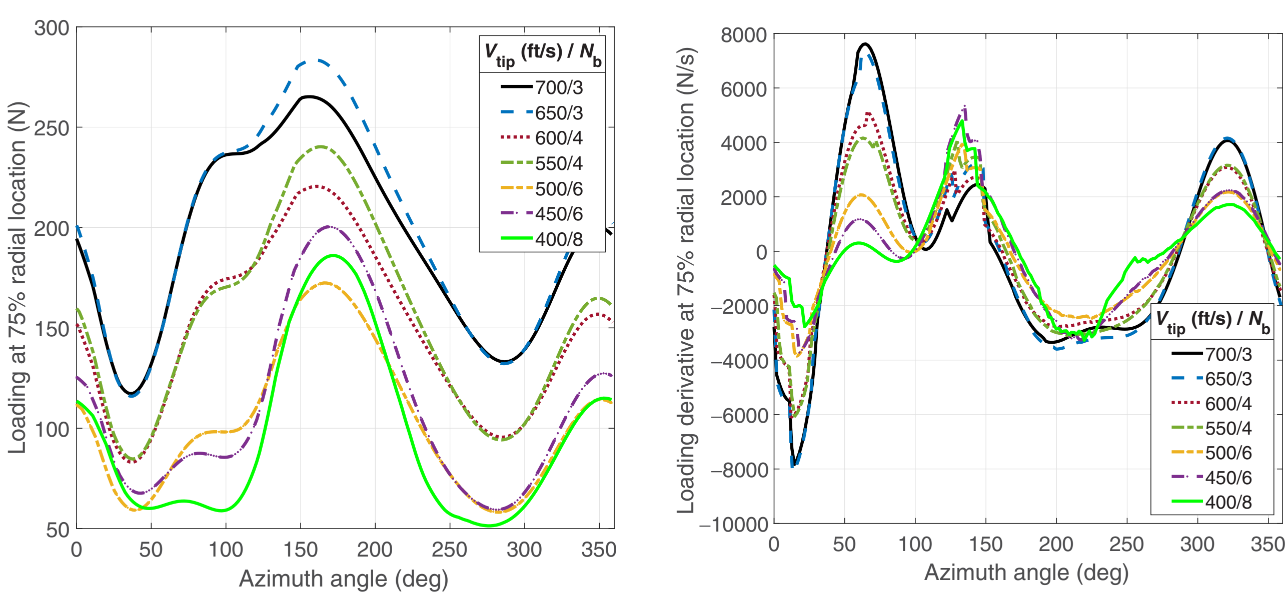

(a) (b)

Fig. 7. Aerodynamic predictions for seven designs over one revolution of the single blade at the 75% radial section: (a) loading force and (b) loading derivative.

Table 2. Quiet air taxi rotor design configurations (Ref. 3)

Rotational Tip Speed (ft/s)	700	650	600	550	500	450	400
Rotor radius (ft)	16.96	17.07	17.09	17.25	17.27	17.64	18.39
Number of blades	3	3	4	4	6	6	8
Solidity	0.0411	0.0477	0.0559	0.0666	0.0805	0.0994	0.1258
Advance ratio	0.246	0.269	0.29	0.319	0.361	0.395	0.411
Blade passing frequency (Hz)	19.7	18.2	22.4	20.3	27.6	24.4	27.7

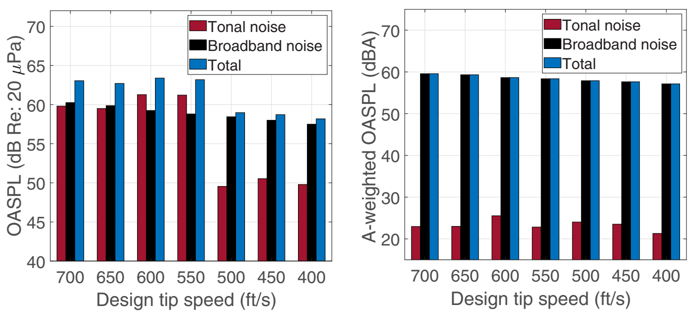

(a) (b)

Fig. 8. Predictions of tonal and broadband noise of the quiet air taxi designs at −90° elevation angle and 492 ft observer-hub distance: (a) OASPL and (b) A-weighted OASPL.

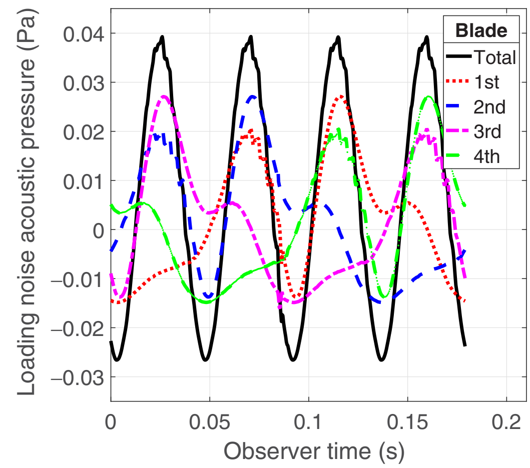

Fig. 9. The loading noise acoustic pressure time histories from each blade and the entire rotor (total) for the design tip speed of 600 ft/s. The observer is at −90° elevation angle and 492 ft observer-hub distance.

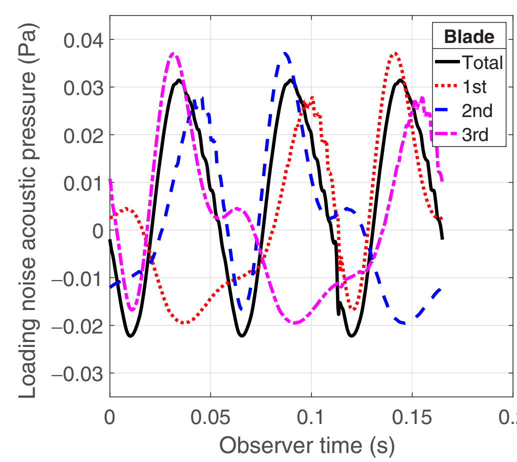

Fig. 10. The loading noise acoustic pressure time histories from each blade and from the entire rotor (total) for the design tip speed of 650 ft/s. The observer is at −90° elevation angle and 492 ft observer-hub distance.

of blades from four blades to six blades, which significantly reduces the blade loading and the associated loading noise. Our study provides more in-depth analyses on the noise trends of the quiet helicopter in flyover and the detailed breakdown of noise contributions, which will continue to be discussed in the subsequent paragraphs and subsections.

The acoustic pressures of the loading noise predicted on the cases of design tip speeds of 600 ft/s (four blades) and 650 ft/s (three blades) are shown in Figs. 9 and 10, where the time windows of one rotor revolution are used. The loading noise acoustic pressure contributions from each individual blade as well as the total acoustic pressure are shown in the same observer time range. It is observed that although the acoustic pressure peak of a single blade of the 600-ft/s tip speed case is lower than that of the 650-ft/s tip speed case, the 600-ft/s tip speed case has the higher total loading noise acoustic pressure when including all the blades due to the constructive interference. The destructive interference is seen on the 650-ft/s tip speed case, where the positive pressure peak of one blade is superimposed with the negative pressure peak of another blade at the same observer time. Note that the destructive interference depends on the observer position, and this effect may not appear at other observer positions.

The narrow-band SPL predictions of broadband noise for the air taxi conceptual designs are given in Fig. 11, where the high-frequency noise level increases with the higher design tip speeds. Below 1 kHz, the minimum broadband noise level is found at the tip speed of 500 ft/s, which resulted from the combined effects of the number of blades and the design tip speeds. However, the difference in the broadband noise level at low frequencies among various designs is small. It is also confirmed that the broadband noise peaks are near 2 kHz frequency, which is the most sensitive frequency range for human hearing.

At a different observer location of −45° elevation angle and observer–hub distance of 492 ft in front of the rotor, tonal noise and broadband noise are predicted for the seven conceptual designs as shown in Fig. 12. Compared to the observer directly beneath the rotor, the observer at −45° elevation angle experiences significantly higher tonal noise due to the presence of the thickness noise that propagates in the forward direction. The broadband noise level is reduced at −45° elevation angle compared to −90° since rotor broadband noise has the dipole directivity pattern with the maximum noise level at −90° elevation angle (Ref. 22). Broadband noise is significantly higher than tonal noise at 400 ft/s. A-weighting still shows the dominance of broadband noise in Fig. 12(b). Figure 13 shows that as the design tip speed is increased, low-frequency broadband noise decreases while high-frequency broadband noise increases. When the design tip speed is reduced, the blade chord length and the number of

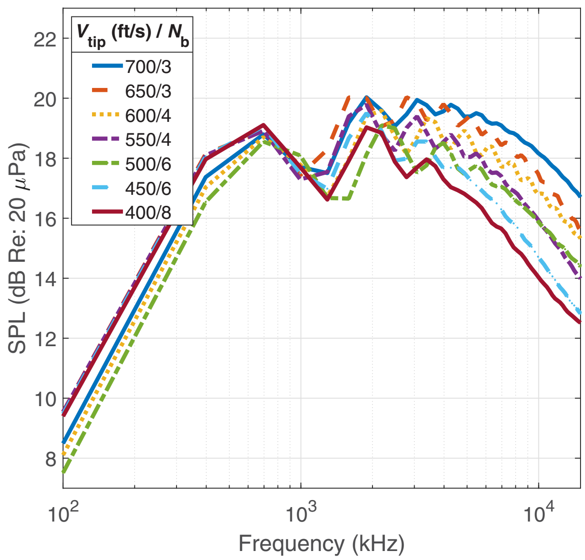

Fig. 11. Narrow-band SPL predictions of broadband noise for the seven design cases at the elevation angle of −90° and 492 ft observer–hub distance.

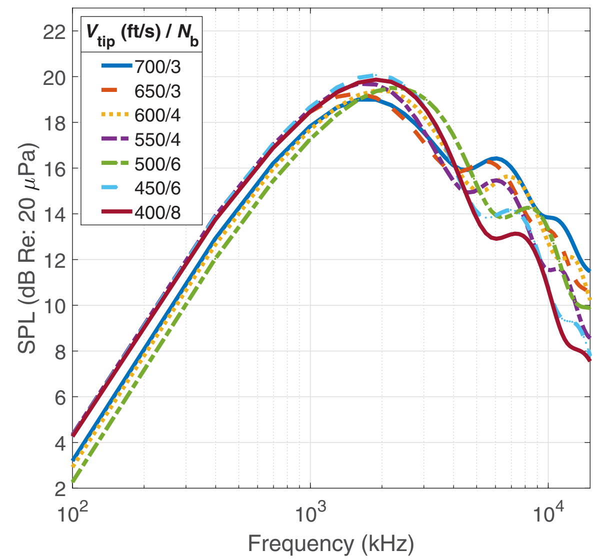

Fig. 13. Narrow-band SPL predictions of broadband noise for the seven design cases at the elevation angle of −45° and 492 ft observer–hub distance at the forward position of the vehicle.

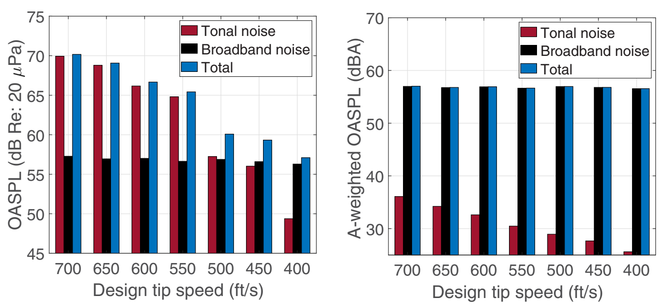

Fig. 12. Predictions of tonal and broadband noise of the quiet air taxi designs at −45° elevation angle and 492 ft observer–hub distance: (a) OASPL and (b) A-weighted OASPL.

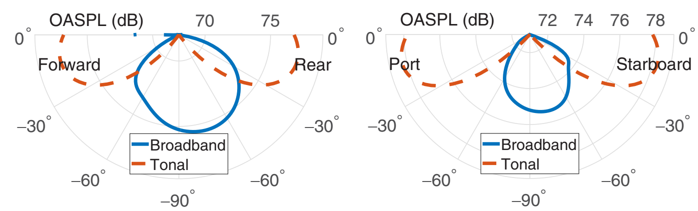

Fig. 14. Noise directivity in the vehicle downward region of the design tip speed of 450 ft/s and the observer–hub distance of 5 rotor radii, with the elevation angle in the longitudinal and lateral directions shown in the polar angle: (a) port side view and (b) rear view.

blades are increased, and the larger chord length results in the increase in the boundary layer thickness near the trailing edge and increases low-frequency broadband noise. Although Fig. 13 shows the opposite trends for the low- and high-frequency ranges, the broadband noise OASPL uniformly increases with increasing the tip speed.

The tonal and broadband noise directivities of the 450 ft/s tip speed design are shown in Fig. 14 where the observer–hub distance is 5 rotor radii or 88.2 ft. This observer distance is much larger than the acoustics wavelength of 5.62 ft at 0.2 kHz, well below the frequency of interest in this study, and hence the far-field assumption in the broadband predictions is satisfied. With the same observer–hub distance, it is shown that the rear side has a higher broadband noise level than the forward side, since the motion of a source and an observer reduces the noise propagation distance towards the rear side and increases the propagation distance towards the forward side as the observer is attached to the rotor in forward flight. In Fig. 14(b), broadband noise is biased towards the starboard side since the advancing blade has a higher local velocity (tip speed) than the retreating blade. Although the retreating blade experiences a higher local angle of attack, broadband noise does not increase much since the flow velocity effect is more dominant than the angle of attack for broadband noise. Tonal noise is observed to be dominant in the in-plane directions, primarily contributed by the presence of the thickness noise. Comparing their relative importance, broadband noise is more important to the observer underneath the vehicle while tonal noise is dominant in the forward direction. Tonal noise is shown to have the same directivity patterns in the forward and rear directions. Note that the broadband noise OASPL shown in Fig. 14 is not weighted, and A-weighting will greatly reduce the tonal noise level. However, tonal noise is expected to maintain its dominance for the in-plane observers at a long observer distance since atmospheric absorption attenuates high-frequency broadband noise at large distances, which is not considered in the current study.

The sectional OASPL contours of broadband noise generated by one blade over the rotation are shown in Fig. 15 to understand the noise distribution on the rotor disk. The rotor flight conditions are given in Table 2, and the observer is 492 ft away from the rotor hub at the elevation angle of −90°. The noise contours show that the OASPL increases with increasing the design tip speed. The starboard side generates broadband noise of about 10 dB higher than the retreating blade due to the higher flow speed on the advancing blade. Although Fig. 15 shows the noise contribution from one blade, the overall broadband noise from all the blades will provide the same conclusion that the lower design tip speed rotor with more blades results in lower broadband noise as shown in Fig. 8.

The contours of the boundary layer parameters for the 700 ft/s tip speed case are shown in Fig. 16 to understand the broadband noise source

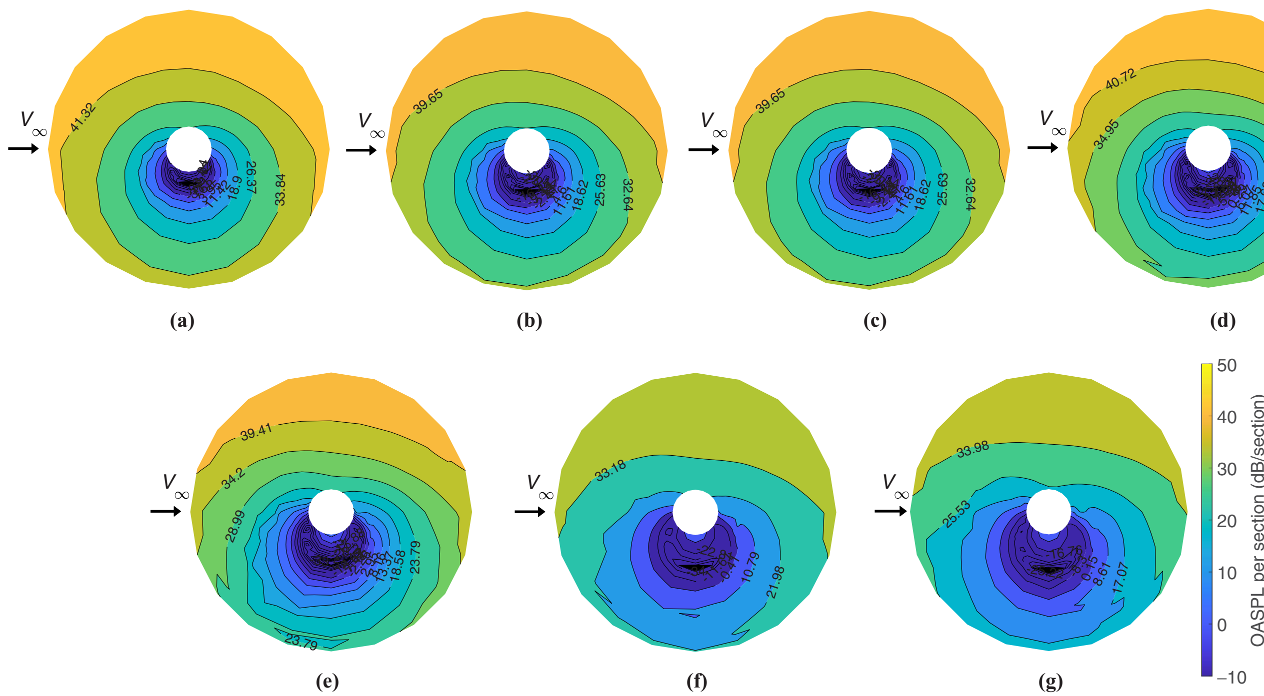

Fig. 15. Sectional OASPL contours at the observer–hub distance of 492 ft and the elevation angle of −90°: (a) 700 ft/s, (b) 650 ft/s, (c) 600 ft/s, (d) 550 ft/s, (e) 500 ft/s, (f) 450 ft/s, and (g) 400 ft/s.

distributions. Note that the boundary layer parameters, such as the boundary layer edge velocity, boundary layer thickness, pressure gradient, skin friction coefficient, etc., are used in Lee's empirical wall pressure spectrum model (Ref. 44), which is an input to the Amiet trailing-edge noise model (Ref. 40). The parameters are taken at 99% of the chord length, which are used to calculate trailing-edge noise. The advancing side is shown to have significantly larger boundary layer edge velocity than the retreating side, which makes the higher broadband noise level on the advancing side as shown in Fig. 14. The upper surface of the advancing side has smaller displacement thickness values than the retreating side due to the lower cyclic pitch or lower angle of attack. The inboard region on the retreating side shows the large displacement thickness due to the reverse flow, but the noise contribution from this inboard region is relatively small due to the smaller velocity. The pressure gradient contours show a similar trend as the boundary layer edge velocity since the two parameters are proportionally related. The pressure gradient contours show a discontinuity at the blade tip section where the two different airfoils are connected at the 90% radial position: VR12 airfoil inboard of 90% and SSCA09 airfoil outboard. Since the values of the skin friction coefficient are not in the same order of magnitude on the rotor disk, especially in the inboard region of the retreating side, the contours of $\log(C_f)$ are depicted in Fig. 16. It is shown that the skin friction coefficient has a complex trend on the upper surface, and the discontinuity near the tip region comes from the change of the airfoils. The effect of the boundary layer edge velocity is more dominant than the skin friction coefficient for trailing-edge noise.

Effect of advance ratio

The air taxi configuration of 450 ft/s blade tip speed is used to study the effect of advance ratio on its acoustics. The observer is 492 ft from the rotor hub with the elevation angle of −90° (downward position), and the observer moves along with the vehicle. The advance ratio is varied from 0.25 to the maximum design advance ratio of 0.442. As we use fixed-RPM with variable pitch for the rotor, the higher advance ratio represents the higher forward speed. The rotor trim solutions are found for each value of the advance ratio. It is seen in Fig. 17 that both tonal noise and broadband noise increase proportionally with increasing the advance ratio, and the relative importance between tonal noise and broadband noise remains unchanged. It is interesting to observe that the difference between tonal and broadband noise remains the same for the varied advance ratios, which suggests the same forward-speed scaling for the two noise sources. The narrow-band SPL of broadband noise is shown in Fig. 18 where broadband noise increases in the entire frequency range with increasing the advance ratio. According to the lateral moment balance of the vehicle, the increasing advance ratio results in a higher local velocity and a lower angle of attack on the advancing side, and a lower local velocity and a higher angle of attack on the retreating side. Since the flow speed is the primary effect on broadband noise, the increased velocity on the advancing side contributes to higher broadband noise. In addition, tonal noise increases with the higher forward speed due to the larger blade loading and loading derivative on the advancing blade.

Broadband noise amplitude modulation and psychoacoustics

The amplitude modulations of broadband noise are calculated on the seven air taxi designs listed in Table 2, and the time range for all the test cases is 2 rotor revolutions. The observer is 5 rotor radii from the rotor hub, and the elevation angle is −45° in the forward direction. The time variations of the noise spectrum are shown in Fig. 19, where the number of noise peaks corresponds to the number of blade passages in two revolutions. The noise spectrum shows that the characteristics of the modulations diminish with increasing the number of blades and decreasing the design tip speed. To quantify the significance of the fluctuations in the psychoacoustic perspective, the fluctuation strength and the roughness of the seven cases are calculated using Eqs. (12) and (13) in and shown Figs. 20 and 21. Although the 650-ft/s tip speed design

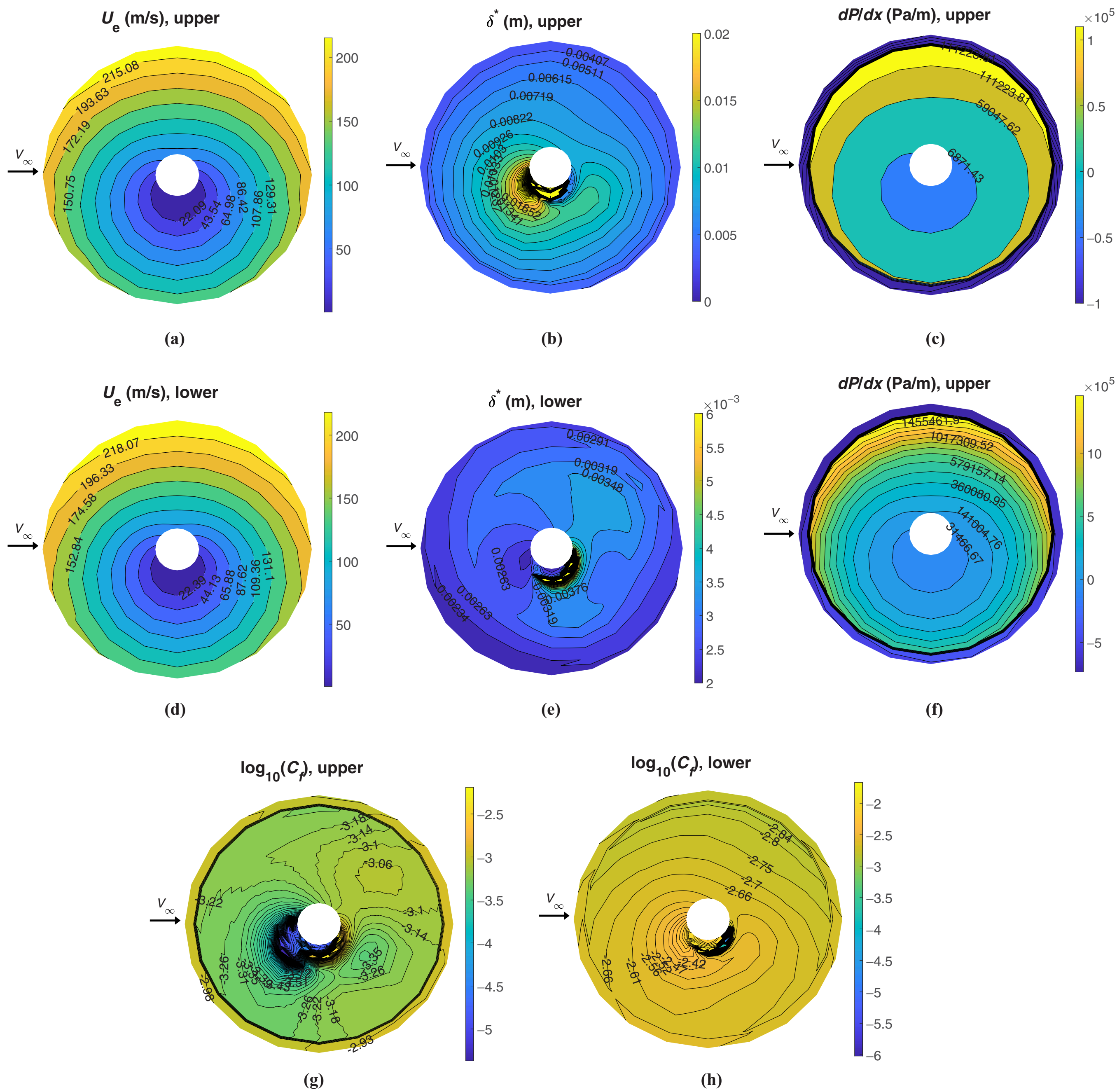

Fig. 16. Contours of the boundary layer parameters taken at 99% of the blade chord length for the 700 ft/s tip speed case: (a) boundary layer edge velocity on the upper surface, (b) displacement thickness on the upper surface, (c) chord-wise pressure gradient on the upper surface, (d) boundary layer edge velocity on the lower surface, (e) displacement thickness on the lower surface, (f) chord-wise pressure gradient on the lower surface, (g) skin friction coefficient on the upper surface, and (h) skin friction coefficient on the lower surface.

has lower noise levels than the 700-ft/s case, its blade passing frequency is lower than the latter; hence its fluctuation strength is higher in Fig. 20. Figure 20 also shows that the fluctuation strength becomes negative, or negligible, for the design tip speed lower than 600 ft/s, which occurs when the modulation depth ΔL is less than 3.52 dB as discussed in Eq. (12). These small modulation depths are attributed to two factors. First, the maximum noise peaks are reduced for the low tip speed cases. Second, the high modulation frequencies with more blades make the edge of the noise signature of one blade closely overlap with those of its adjacent blades so that the modulation events are less visible as shown in Fig. 19. Figure 21 shows that the rotor designs with the higher tip speeds and fewer blades create a more severe sensation of roughness. Given that all seven cases achieve the same missions, low-RPM rotors with more blades are preferable from a psychoacoustic point of view. Note that fluctuation and roughness considered in this paper are two factors to evaluate the annoyance of rotorcraft noise, and other factors, such as loudness and tonality, can also affect the annoyance level (Ref. 64).

Conclusions

The rotorcraft acoustics analysis procedure in forward flight was developed to predict both tonal noise and broadband noise as well as

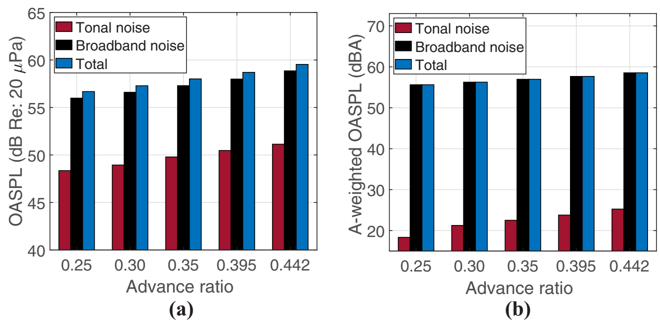

Fig. 17. Predictions of tonal and broadband noise of the 450 ft/s tip speed design for varied advance ratios at −90° elevation angle and 492 ft observer–hub distance: (a) OASPL, and (b) A-weighted OASPL.

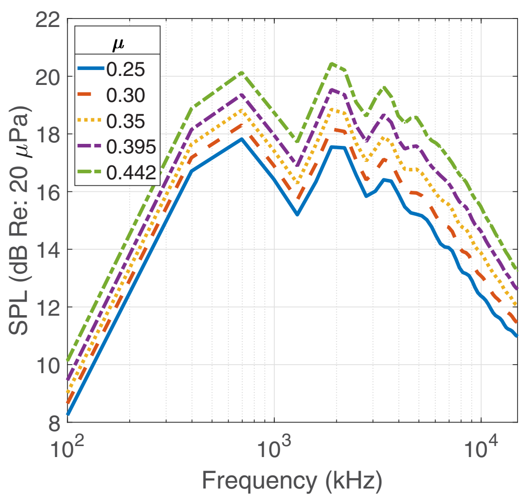

Fig. 18. Narrow-band SPL predictions of broadband noise of the 450 ft/s tip speed design for varied advance ratios at −90° elevation angle and 492 ft observer–hub distance.

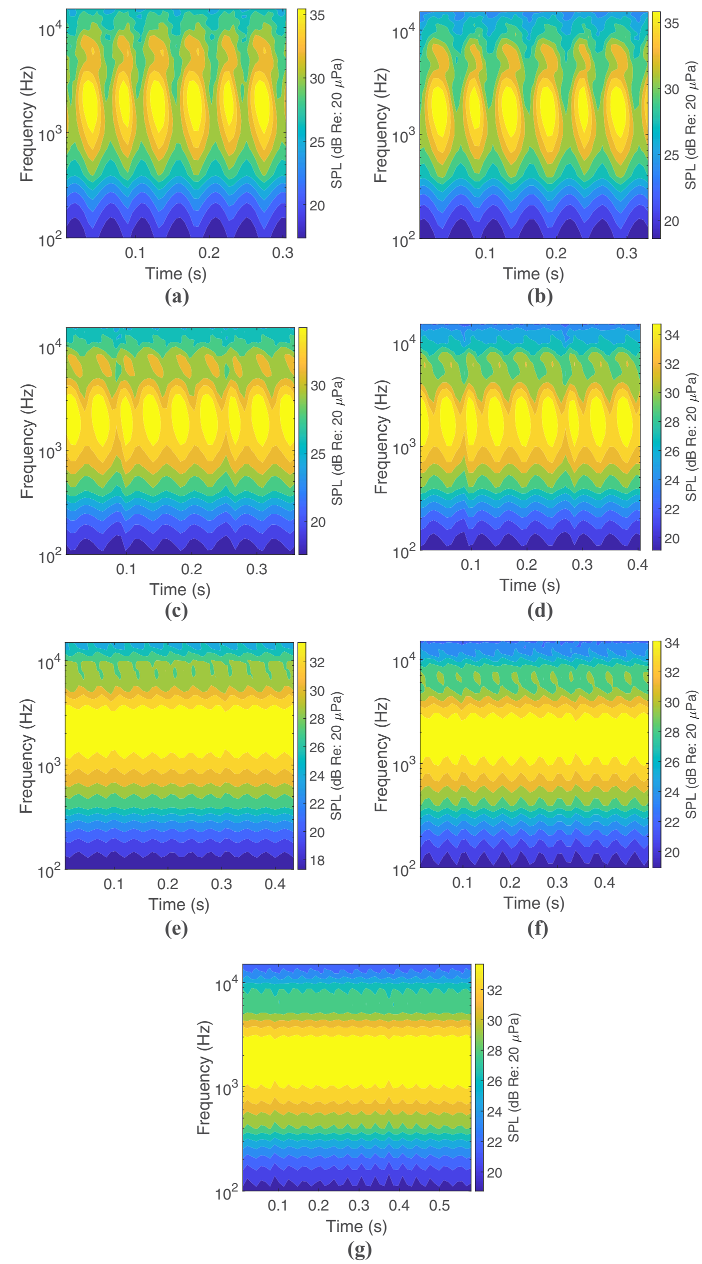

Fig. 19. Time variation of the broadband noise spectrum at 5 rotor radii observer distance and −45° forward elevation angle for the design tip speeds of: (a) 700 ft/s, (b) 650 ft/s, (c) 600 ft/s, (d) 550 ft/s, (e) 500 ft/s, (f) 450 ft/s, and (g) 400 ft/s.

psychoacoustics. This method couples the dynamic-inflow blade element theory, PSU-WOPWOP, and UCD-QuietFly. The acoustic sources included in this study are the thickness noise, loading noise, trailing-edge noise, trailing-edge bluntness noise, and stall noise. The numerical method was applied to investigate the acoustics of a quiet helicopter with seven rotor designs. The major findings are summarized as follows:

1) At the downward observer, broadband noise is the dominant noise source for the rotor designs with low tip speeds and more blades, while broadband noise and tonal noise have comparable noise levels for the rotors with high tip speeds and fewer blades. In the forward region of the rotor, tonal noise is the dominant noise source for the high-tip-speed design, while broadband noise and tonal noise have comparable noise levels for the rotors with low tip speeds.

2) On the A-weighted sound pressure spectrum, broadband noise is demonstrated to be the dominant noise source in the out-of-plane directions. Note that BVI noise and atmospheric absorption are not included in the current study, which may alter this conclusion when these effects are important.

3) Broadband noise is demonstrated to be biased towards the rear and starboard directions due to the motion of a source and an observer and the higher velocity on the advancing blade. The noise contribution contours show the higher broadband noise contributions from the advancing side, primarily due to the boundary layer edge velocity.

4) In the study of the effect of the advance ratio on the rotor acoustics, the relative importance of tonal noise and broadband noise remains unchanged for varying forward speeds. Both the tonal and broadband noise levels are shown to increase proportionally with increasing the advance ratio.

5) Psychoacoustic metrics of the fluctuation strength and roughness were calculated based on the amplitude modulation of broadband noise. It was shown that the fluctuation strength was negligible when the modulation depth is less than 3.52 dB, which is more distinct at the high blade passing frequency with more blades. The sensations of both the

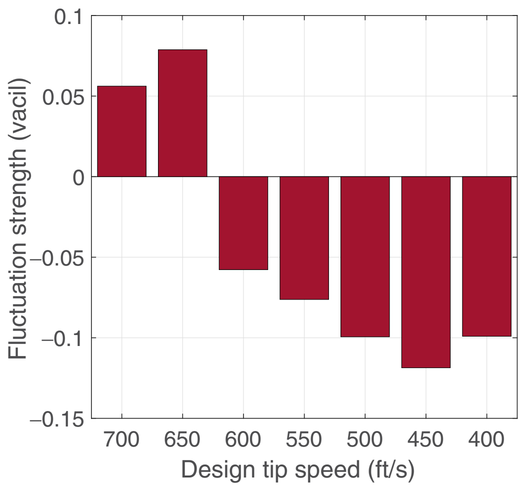

Fig. 20. Fluctuation strengths of the rotor designs at 5 rotor radii observer distance and −45° forward elevation angle.

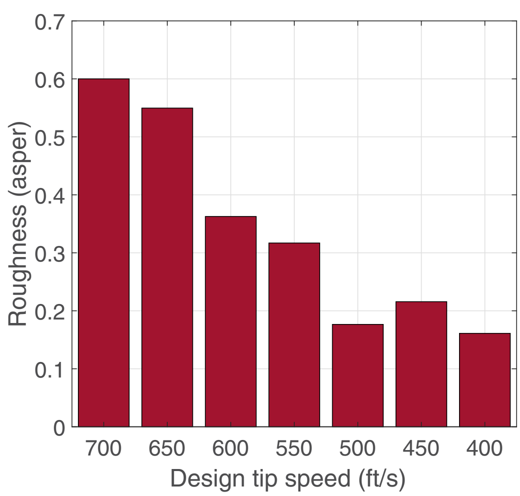

Fig. 21. Roughness of the rotor designs at 5 rotor radii observer distance and −45° forward elevation angle.

fluctuation and roughness reduce with the decrease in the design tip speed. Therefore, the rotor designs with a low tip speed and more blades are preferable in terms of psychoacoustic metrics.

References

[1]Silva, C., Johnson, W., Solis, E., Patterson, M., and Antcliff, K., "VTOL Urban Air Mobility Concept Vehicles for Technology Development," AIAA 2018-3847, Proceedings of the 2018 AIAA Aviation Forum, Atlanta, GA, June 25–29, 2018.

[2]Hendricks, E. S., Aretskin-Hariton, E., Ingraham, D., Gray, J. S., Schnulo, S. L., Chin, J., Falck, R., and Hall, D., "Multidisciplinary Optimization of an Electric Quadrotor Urban Air Mobility Aircraft," AIAA 2020-3176, Proceedings of the 2020 AIAA Aviation Forum, 2020, Virtual Event, June 15–19, 2020.

[3]Johnson, W., "A Quiet Helicopter for Air Taxi Operations," Proceedings of the 2020 VFS Aeromechanics for Advanced Vertical Flight Technical Meeting, San Jose, CA, January 21–23, 2020.

[4]Scott, M., "Military Mission Suitability Assessment of eVTOL Aircraft Configurations," Proceedings of the Vertical Flight Society 77th Annual Forum & Technology Display, Virtual Event, May 10–14, 2021.

[5]Sherman, J., "Urban Air Mobility Steals the Show at CES 2020," *Vertiflite*, Vol. 64, (4), 2020, pp. 62–63.

[6]Stoll, A., Bevirt, B., Pei, P., and Stilson, E., "Conceptual Design of the Joby S2 Electric VTOL PAV," AIAA 2014-2407, Proceedings of the 2014 AIAA Aviation Forum, Atlanta, GA, June 16–20, 2014.

[7]Hasan, S., "Urban Air Mobility (UAM) Market Study," NASA Report HQ-E-DAA-TN63497s, NASA Headquarters, Washington, DC, November 1, 2018.

[8]Holden, J., and Goel, N., "Fast-Forwarding to a Future of On-Demand Urban Air Transportation," White Paper, Uber, 2016.

[9]Li, S., and Lee, S., "Prediction of Urban Air Mobility Multirotor VTOL Broadband Noise Using UCD-QuietFly," *Journal of the American Helicopter Society*, Vol. 66, (3), 2021, pp. 1–13.

[10]Jia, Z., and Lee, S., "High-Fidelity Computational Analysis on the Noise of a Side-by-Side Hybrid VTOL Aircraft," *Journal of the American Helicopter Society*, April, 2022.

[11]Sagaga, J., and Lee, S., "Acoustic Predictions for the Side-by-Side Air Taxi Rotor in Hover," Proceedings of the Vertical Flight Society 77th Annual Forum & Technology Display, Virtual Event, May 10–14, 2021.

[12]Jia, Z., and Lee, S., "Acoustic Analysis of a Quadrotor eVTOL Design via High-Fidelity Simulations," AIAA 2019-2631, Proceedings of the 25th AIAA/CEAS Aeroacoustics Conference, Delft, The Netherlands, May 20–23, 2019.

[13]Jia, Z., and Lee, S., "Computational Study on Noise of Urban Air Mobility Quadrotor Aircraft," *Journal of the American Helicopter Society*, **67**, 012009 (2022).

[14]Pettingill, N., and Zawodny, N., "Identification and Prediction of Broadband Noise for a Small Quadcopter," Proceedings of the Vertical Flight Society 75th Annual Forum & Technology Display, Philadelphia, PA, May 13–16, 2019.

[15]Brooks, T., Pope, D., and Marcolini, M., "Airfoil Self-noise and Prediction," NASA RP 1218, 1989.

[16]Thurman, C., Zawodny, N., and Baeder, J., "Computational Prediction of Broadband Noise from a Representative Small Unmanned Aerial System Rotor," Proceedings of the Vertical Flight Society 76th Annual Forum, Virtual Event, October 5–8, 2020.

[17]Smith, B., Gandhi, F., and Niemiec, R., "A Comparison of Multicopter Noise Characteristics with Increasing Number of Rotors," Proceedings of the Vertical Flight Society 76th Annual Forum, Virtual Event, October 5–8, 2020.

[18]Niemiec, R., and Gandhi, F., "Development and Validation of the Rensselaer Multicopter Analysis Code (RMAC): A Physics-Based Comprehensive Modeling Tool," Proceedings of the Vertical Flight Society 75th Annual Forum & Technology Display, Philadelphia, PA, May 13–16, 2019.

[19]Bres, G., Brentner, K., Perez, G., and Jones, H., "Maneuvering rotorcraft noise prediction," *Journal of Sound and Vibration*, Vol. 275, (3–5), 2004, pp. 719–738.

[20]Lee, S., Brentner, K., Farassat, F., and Morris, P., "Analytic Formulation and Numerical Implementation of an Acoustic Pressure Gradient Prediction," *Journal of Sound and Vibration*, Vol. 319, (3), 2009, pp. 1200–1221.

[21]Jia, Z., Lee, S., Sharma, K., and Brentner, K., "Aeroacoustic Analysis of a Lift-Offset Coaxial Rotor Using High-Fidelity CFD/CSD Loose Coupling Simulation," *Journal of the American Helicopter Society*, **65**, (1), 012011 (2020).

[22]Li, S., and Lee, S., "Prediction of Rotorcraft Broadband Trailing-Edge Noise and Parameter Sensitivity Study," *Journal of the American Helicopter Society*, **65**, 042006 (2020).

[23]Brentner, K., and Farassat, F., "Modeling Aerodynamically Generated Sound of Helicopter Rotors," *Progress in Aerospace Sciences*, Vol. 39 (2), 2003, pp. 83–120.

[24]Farassat, F., and Succi, G., "The Prediction of Helicopter Discrete Frequency Noise," *Vertica*, Vol. 7, (4), 1983, pp. 309–320.

[25]Ffowcs Williams, J., and Hawkings, D., "Theory Relating to the Noise of Rotating Machinery," *Journal of Fluid Mechanics*, Vol. 10, (1), 1969, pp. 10–21.

[26]Lopes, L., and Burley, C., "Design of the Next Generation Aircraft Noise Prediction Program: ANOPP2," AIAA 2011-2854, Proceedings of the 17th AIAA/CEAS Aeroacoustics Conference, Portland, OR, June 5–8, 2011.

[27]Lee, S., Brentner, K., and Morris, P., "Long-Range and Nonlinear Propagation of Helicopter High-Speed Impulsive Noise," *Journal of the American Helicopter Society*, Vol. 62, (2), 2017, pp. 1–10.

[28]Brooks, T., Marcolini, M., and Pope, D., "Main Rotor Broadband Noise Study in the DNW," *Journal of the American Helicopter Society*, Vol. 34, (2), 1989, pp. 3–12.

[29]Stephenson, J., Watts, M., Greenwood, E., and Pascioni, K., "Development and Validation of Generic Maneuvering Flight Noise Abatement Guidance for Helicopters," *Journal of the American Helicopter Society*, Vol. 67, (1), 2022, pp. 1–12.

[30]Reboul, G., Bailly, J., Rottmann, L., Bekemeyer, P., Einarsson, G., and Guntzer, F., "Prediction of RACER's Lateral Rotor Noise Using the CONCERTO Chain," Proceedings of the Vertical Flight Society 77th Annual Forum & Technology Display, Virtual Event, May 10–14, 2021.

[31]Sharma, K., Brentner, K., Jia, Z., Lee, S., and Anusonti-Inthra, P., "Aeroacoustic Predictions of the Free-Wake Model, Vortex Particle Method, and Computational Fluid Dynamics for a Coaxial Rotor System," Proceedings of the Vertical Flight Society 75th Annual Forum & Technology Display, Philadelphia, PA, May 13–16, 2019.

[32]Jacobellis, G., Singh, R., Johnson, C., Sirohi, J., and McDonald, R., "Experimental and Computational Investigation of Stacked Rotor Acoustics in Hover," Proceedings of the Vertical Flight Society 76th Annual Forum, Virtual Event, October 5–8, 2020.

[33]Botre, M., Brentner, K., Horn, J., and Wachspress, D., "Validation of Helicopter Noise Prediction System with Flight Data," Proceedings of the Vertical Flight Society 75th Annual Forum & Technology Display, Philadelphia, PA, May 13–16, 2019.

[34]He, C., Ware, C., Yang, S., Kim, J., Baeder, J., and Jung, Y., "eVTOL Rotor Noise Study Using Comprehensive Modeling Combined with Acoustic Analysis," Proceedings of the Vertical Flight Society 77th Annual Forum & Technology Display, Virtual Event, May 10–14, 2021.

[35]Smith, B., Gandhi, F., and Lyrintzis, A., "An Assessment of Multicopter Noise in Edgewise Flight," Proceedings of the Vertical Flight Society 77th Annual Forum & Technology Display, Virtual Event, May 10–14, 2021.

[36]Akiwate, D. C., Parry, A. B., Joseph, P., and Paruchuri, C. C., "On the Balance between the Tonal and Broadband Noise of Uninstalled Propellers," AIAA 2021-2308, Proceedings of the 2021 AIAA Aviation Forum, Virtual Event, August 2–6, 2021.

[37]Snider, R., Samuels, T., Goldman, B., and Brentner, K., "Full-Scale Rotorcraft Broadband Noise Prediction and Its Relevance to Civil Noise Certification Criteria," Proceedings of the 69th Annual Forum of the American Helicopter Society, Phoenix, AZ, May 21–23, 2013.

[38]Intaratep, N., Alexander, W., and Devenport, W., "Experimental Study of Quadcopter Acoustics and Performance at Static Thrust Conditions," AIAA 2016-2873, Proceedings of the 22nd AIAA/CEAS Aeroacoustics Conference, Lyon, France, May 30–June 1, 2016.

[39]Zawodny, N., and Boyd, D., "Investigation of Rotor-Airframe Interaction Noise Associated with Small-Scale Rotary-Wing Unmanned Aircraft Systems," *Journal of the American Helicopter Society*, **65**, 012007 (2020).

[40]Amiet, R., "Noise Due to Turbulent Flow Past a Trailing Edge," *Journal of Sound and Vibration*, Vol. 47, (3), 1976, pp. 387–393.

[41]Howe, M., "Aerodynamic Noise of a Serrated Trailing Edge," *Journal of Fluids and Structures*, Vol. 5, (1), 1991, pp. 33–45.

[42]Lee, S., Ayton, L., Bertagnolio, F., Moreau, S., Chong, T. P., and Joseph, P., "Turbulent Boundary Layer Trailing-Edge Noise: Theory, Computation, Experiment, and Application," *Progress in Aerospace Sciences*, **126**, 100737 (2021).

[43]Ayton, L. J., "Analytic Solution for Aerodynamic Noise Generated by Plates with Spanwise-Varying Trailing Edges," *Journal of Fluid Mechanics*, Vol. 849, 2018, pp. 448–466.

[44]Lee, S., "Empirical Wall-Pressure Spectral Modeling for Zero and Adverse Pressure Gradient Flows," *AIAA Journal*, Vol. 56 (5), 2018, pp. 1818–1829.

[45]Thai, A. D., De Paola, E., Di Marco, A., Stoica, L. G., Camussi, R., Tron, R., and Grace, S. M., "Experimental and Computational Aeroacoustic Investigation of Small Rotor Interactions in Hover," *Applied Sciences*, **11**, 10016 (2021).

[46]Rozenberg, Y., Roger, M., and Moreau, S., "Rotating Blade Trailing-Edge Noise: Experimental Validation of Analytical Model," *AIAA Journal*, Vol. 48, (5), 2010, pp. 951–962.

[47]Zarri, A., Christophe, J., Moreau, S., and Schram, C., "Influence of Swept Blades on Low-Order Acoustic Prediction for Axial Fans," *Acoustics*, Vol. 2, (4), 2020, pp. 812–832.

[48]Lau, A., Kim, J., Hurault, J., Vronsky, T., and Joseph, P., "Aerofoil Trailing-Edge Noise Prediction Models for Wind Turbine Applications," *Wind Energy*, Vol. 20, 2017, pp. 1727–1752.

[49]Li, S., and Lee, S., "Predictions and Validations of Small-Scale Rotor Noise Using UCD-QuietFly," Proceedings of the Vertical Flight Society 2022 Transformative Vertical Flight - Aeromechanics for Advanced Vertical Flight Technical Meeting, San Jose, CA, January 25–27, 2022.

[50]Pettingill, N., Zawodny, N., Thurman, C., and Lopes, L., "Acoustic and Performance Characteristics of an Ideally Twisted Rotor in Hover," AIAA 2021-1928, Proceedings of the 2021 AIAA SciTech Forum, Virtual Event, January 19–21, 2021.

[51]Jung, Y., Baeder, J., and He, C., "Investigation of Empirical Rotor Broadband Prediction using CFD Boundary Layer Parameters Extraction," Proceedings of the Vertical Flight Society 77th Annual Forum, Virtual Event, May 11–13, 2021.

[52]Gan, Z. F., Brentner, K., and Greenwood, E., "Time Variation of Rotor Broadband Noise," Proceedings of the Vertical Flight Society's 9th Biennial Autonomous VTOL Technical Meeting, Virtual Event, January 26–28, 2021.

[53]Krishnamurthy, S., Rizzi, S. A., Cheng, R., Boyd, D. D., and Christian, A. W., "Prediction-Based Auralization of a Multirotor Urban Air Mobility Vehicle," AIAA 2021-0587, Proceedings of the 2021 AIAA SciTech Forum, Virtual Event, January 19–21, 2021.

[54]Silva, C., and Johnson, W., "Practical Conceptual Design of Quieter Urban VTOL Aircraft," Proceedings of the Vertical Flight Society 77th Annual Forum & Technology Display, Virtual Event, May 10–14, 2021.

[55]Drela, M., "XFOIL: An Analysis and Design System for Low Reynolds Number Airfoils," *Low Reynolds Number Aerodynamics*, edited by T. J. Mueller, Lecture Notes in Engineering, vol. 54, Springer, Berlin, Germany, 1989, pp. 1–12.

[56]Peters, D., Boyd, D., and He, C., "Finite-State Induced-Flow Model for Rotors in Hover and Forward Flight," *Journal of the American Helicopter Society*, Vol. 34, (5), 1989, pp. 5–17.

[57]Johnson, W., *Helicopter Theory*, Dover Publication, New York, NY, 1994.

[58]Li, S., and Lee, S., "A Machine Learning-Based Fast Prediction of Rotorcraft Broadband Noise," AIAA 2020-2588, Proceedings of the 2020 AIAA Aviation Forum, Virtual Event, June 15–19, 2020.

[59]Yang, T., Brentner, K., and Walsh, G., "A Dual Compact Model for Rotor Thickness Noise Prediction," *Journal of the American Helicopter Society*, Vol. 63, (2), 2018, pp. 12–23.

[60]Isom, M., "The Theory of Sound Radiated by a Hovering Transonic Helicopter Blade," Report Poly-AE/AM No. 75-4, Polytechnic Institute of New York, Brooklyn, NY, 1975.

[61]Fastl, H., and Zwicker, *Psychoacoustics: Facts and Models*, Springer Series in Information Sciences Book, vol. 22, Springer, Berlin, 2007.

[62]Elliott, J., and Althoff, S., "Inflow Measurement Made with a Laser Velocimeter on a Helicopter Model in Forward Flight," NASA Technical Report 100541-100545, 1988.

[63]Li, S., "Development of Rotorcraft Forward Flight Analysis Code Using the Finite-State Dynamic Inflow Model," Master's thesis, University of California Davis, August 2020.

[64]Boucher, M., Krishnamurthy, S., Christian, A., and Rizzi, S. A., "Sound Quality Metric Indicators of Rotorcraft Noise Annoyance Using Multilevel Regression Analysis," *The Journal of the Acoustical Society of America*, Vol. 145, (3), 2019, pp. 1899–1899.